

Geophysics, 73 , no. 6, S229-S239, (2008))

# Isotropic angle-domain elastic reverse-time migration<sup>a</sup>

---

<sup>a</sup>Published in (

*Jia Yan and Paul Sava*  
*Center for Wave Phenomena*  
*Colorado School of Mines<sup>1</sup>*

---

<sup>1</sup>**e-mail:** [jyan@mines.edu](mailto:jyan@mines.edu), [psava@mines.edu](mailto:psava@mines.edu)

## ABSTRACT

Multicomponent data are not usually processed with specifically designed procedures, but with procedures analogous to the ones used for single-component data. In isotropic media, the vertical and horizontal components of the data are commonly taken as proxies for the P- and S-wave modes which are imaged independently with acoustic wave equations. This procedure works only if the vertical and horizontal component accurately represent P- and S-wave modes, which is not true in general. Therefore, multicomponent images constructed with this procedure exhibit artifacts caused by the incorrect wave mode separation at the surface.

An alternative procedure for elastic imaging uses the full vector fields for wavefield reconstruction and imaging. The wavefields are reconstructed using the multicomponent data as a boundary condition for a numerical solution to the elastic wave equation. The key component for wavefield migration is the imaging condition that evaluates the match between wavefields reconstructed from sources and receivers. For vector wavefields, a simple component-by-component cross-correlation between two wavefields leads to artifacts caused by crosstalk between the unseparated wave modes. An alternative method is to separate elastic wavefields after reconstruction in the subsurface and implement the imaging condition as cross-correlation of pure wave modes instead of the Cartesian components of the displacement wavefield. This approach leads to images that are easier to interpret, since they describe reflectivity of specified wave modes at interfaces of physical properties.

As for imaging with acoustic wavefields, the elastic imaging condition can be formulated conventionally (cross-correlation with zero lag in space and time), as well as extended to non-zero space and time lags. The elastic images produced by an extended imaging condition can be used for angle decomposition of primary (PP or SS) and converted (PS or SP) reflectivity. Angle gathers constructed with this procedure have applications for migration velocity analysis and amplitude versus angle analysis.

## INTRODUCTION

Seismic processing is usually based on acoustic wave equations, which assume that the Earth represents a liquid that propagates only compressional waves. Although useful in practice, this assumption is not theoretically valid. Earth materials allow for both compressional and shear wave propagation in the subsurface. Shear waves, either generated at the source or converted from compressional waves at various interfaces in the subsurface, are detected by multicomponent receivers. Shear waves are usually stronger at large incidence and reflection angles, often corresponding to large offsets. However, for complex geological structures near the surface, shear waves can be quite significant even at small offsets. Conventional single-component imaging ignores shear

wave modes, which often leads to incorrect characterization of wave-propagation, incomplete illumination of the subsurface and poor amplitude characterization.

Even when multicomponent data are used for imaging, they are usually not processed with specifically designed procedures. Instead, those data are processed with ad-hoc procedures borrowed from acoustic wave equation imaging algorithms. For isotropic media, a typical assumption is that the recorded vertical and in plane horizontal components are good approximations for the P- and S-wave modes, respectively, which can be imaged independently. This assumption is not always correct, leading to errors and noise in the images, since P- and S-wave modes are normally mixed on all recorded components. Also, since P and S modes are mixed on all components, true-amplitude imaging is questionable no matter how accurate the wavefield reconstruction and imaging condition are.

Multicomponent imaging has long been an active research area for exploration geophysicists. Techniques proposed in the literature perform imaging by using time extrapolation, e.g. by Kirchhoff migration (Kuo and Dai, 1984a; Hokstad, 2000) and reverse-time migration (Whitmore, 1995; Chang and McMechan, 1986, 1994) adapted for multicomponent data. The reason for working in the time domain, as opposed to the depth domain, is that the coupling of displacements in different directions in elastic wave equations makes it difficult to derive a dispersion relation that can be used to extrapolate wavefields in depth (Clayton and Brown, 1979; Clayton, 1981).

Early attempts at multicomponent imaging used the Kirchhoff framework and involve wave-mode separation on the surface prior to wave-equation imaging (Wapenaar et al., 1987; Wapenaar and Haimé, 1990). Kuo and Dai (1984b) perform shot-profile elastic Kirchhoff migration, and Hokstad (2000) performs survey-sinking elastic Kirchhoff migration. Although these techniques represent different migration procedures, they compute travel-times for both PP and PS reflections, and sum data along these travel time trajectories. This approach is equivalent to distinguishing between PP reflection and PS reflections, and applying acoustic Kirchhoff migration for each mode separately. When geology is complex, the elastic Kirchhoff migration technique suffers from drawbacks similar to those of acoustic Kirchhoff migration because ray theory breaks down (Gray et al., 2001).

There are two main difficulties with independently imaging P and S wave modes separated on the surface. The first is that conventional elastic migration techniques either consider vertical and horizontal components of recorded data as P and S modes, which is not always accurate, or separate these wave modes on the recording surface using approximations, e.g. polarization (Pestana et al., 1989) or elastic potentials (Etgen, 1988; Zhe and Greenhalgh, 1997) or wavefield extrapolation in the vicinity of the acquisition surface (Wapenaar et al., 1990; Admundsen and Reitan, 1995). Other elastic reverse time migration techniques do not separate wave modes on the surface and reconstruct vector fields, but use imaging conditions based on ray tracing (Chang and McMechan, 1986, 1994) that are not always robust in complex geology. The second difficulty is that images produced independently from P and S modes are hard to interpret together, since often they do not line-up consistently, thus

requiring image post processing, e.g. by manual or automatic registration of the images (Gaiser, 1996; Fomel and Backus, 2003; Nickel and Sonneland, 2004).

We advocate an alternative procedure for imaging elastic wavefield data. Instead of separating wavefields into scalar wave modes on the acquisition surface followed by scalar imaging of each mode independently, we use the entire vector wavefields for wavefield reconstruction and imaging. The vector wavefields are reconstructed using the multicomponent vector data as boundary conditions for a numerical solution to the elastic wave equation. The key component of such a migration procedure is the imaging condition which evaluates the match between wavefields reconstructed from the source and receiver. For vector wavefields, a simple component-by-component cross-correlation between the two wavefields leads to artifacts caused by crosstalk between the unseparated wave modes, i.e. all P and S modes from the source wavefield correlate with all P and S modes from the receiver wavefield. This problem can be alleviated by using separated elastic wavefields, with the imaging condition implemented as cross-correlation of wave modes instead of cross-correlation of the Cartesian components of the wavefield. This approach leads to images that are cleaner and easier to interpret since they represent reflections of single wave modes at interfaces of physical properties.

As for imaging with acoustic wavefields, the elastic imaging condition can be formulated conventionally (cross-correlation with zero lag in space and time), as well as extended to non-zero space lags. The elastic images produced by extended imaging condition can be used for angle decomposition of PP and PS reflectivity. Angle gathers have many applications, including migration velocity analysis (MVA) and amplitude versus angle (AVA) analysis.

The advantage of imaging with multicomponent seismic data is that the physics of wave propagation is better represented, and resulting seismic images more accurately characterize the subsurface. Multicomponent images have many applications. For example they can be used to provide reflection images where the P-wave reflectivity is small, image through gas clouds where the P-wave signal is attenuated, validate bright spot reflections and provide parameter estimation for this media, Poisson's ratio estimates, and detect fractures through shear-wave splitting for anisotropic media (Li, 1998; Zhu et al., 1999; Knapp et al., 2001; Gaiser et al., 2001; Stewart et al., 2003; Simmons and Backus, 2003). Assuming no attenuation in the subsurface, converted wave images also have higher resolution than pure-mode images in shallow part of sections, because S-waves have shorter wavelengths than P-waves. Modeling and migrating multicomponent data with elastic migration algorithms enables us to make full use of information provided by elastic data and correctly position geologic structures.

This paper presents a method for angle-domain imaging of elastic wavefield data using reverse-time migration (RTM). In order to limit the scope of our paper, we ignore several practical issues related to data acquisition and pre-processing for wave-equation migration. For example, our methodology ignores the presence of surface waves, e.g. Rayleigh and Love waves, the relatively poor spatial sampling when

imaging with multicomponent elastic data, e.g. for OBC acquisition, the presence of anisotropy in the subsurface and all amplitude considerations related to the directionality of the seismic source. All these issues are important for elastic imaging and need to be part of a practical data processing application. We restrict in this paper our attention to the problem of wave-mode separation after wavefield extrapolation and angle-decomposition after the imaging condition. These issues are addressed in more detail in a later section of the paper.

We begin by summarizing wavefield imaging methodology, focusing on reverse-time migration for wavefield multicomponent migration. Then, we describe different options for wavefield multicomponent imaging conditions, e.g. based on vector displacements and vector potentials. Finally, we describe the application of extended imaging conditions to multicomponent data and corresponding angle decomposition. We illustrate the wavefield imaging techniques using data simulated from the Marmousi II model (Martin et al., 2002).

## WAVEFIELD IMAGING

Seismic imaging is based on numerical solutions to wave equations, which can be classified into ray-based (integral) solutions and wavefield-based (differential) solutions. Kirchhoff migration is a typical ray-based imaging procedure which is computationally efficient but often fails in areas of complex geology, such as sub-salt, because the wavefield is severely distorted by lateral velocity variations leading to complex multipathing. Wavefield imaging works better for complex geology, but is more expensive than Kirchhoff migration. Depending on computational time constraints and available resources, different levels of approximation are applied to accelerate imaging, i.e. one-way vs. two-way, acoustic vs. elastic, isotropic vs. anisotropic, etc.

Despite the complexity of various types of wavefield migration algorithms, any wavefield imaging method can be separated into two parts: wavefield reconstruction followed by the application of an imaging condition. For prestack depth migration, source and receiver wavefields have to be reconstructed at all locations in the subsurface. The wavefield reconstruction can be carried out using extrapolation in either depth or time, and with different modeling approaches, such as finite-differences (Dablain, 1986; Alford et al., 1974), finite-elements (Bolt and Smith, 1976), or spectral methods (Seriani and Priolo, 1991; Seriani et al., 1992; Dai and Cheadle, 1996). After reconstructing wavefields with the recorded data as boundary conditions into the subsurface, an imaging condition must be applied at all locations in the subsurface in order to obtain a seismic image. The simplest types of imaging conditions are based on cross-correlation or deconvolution of the reconstructed wavefields (Claerbout, 1971). These imaging conditions can be implemented in the time or frequency domain depending on the domain in which wavefields have been reconstructed. Here, we concentrate on reverse-time migration with wavefield reconstruction and imaging condition implemented in the time domain.

## Reverse-time migration

Reverse-time migration reconstructs the source wavefield forward in time and the receiver wavefield backward in time. It then applies an imaging condition to extract reflectivity information out of the reconstructed wavefields. The advantages of reverse-time migration over other depth migration techniques are that the extrapolation in time does not involve evanescent energy, and no dip limitations exist for the imaged structures (McMechan, 1982, 1983; Whitmore, 1983; Baysal et al., 1983). Although conceptually simple, reverse-time migration has not been used extensively in practice due to its high computational cost. However, the algorithm is becoming more and more attractive to the industry because of its robustness in imaging complex geology, e.g. sub-salt (Jones et al., 2007; Boechat et al., 2007).

McMechan (1982, 1983), Whitmore (1983) and Baysal et al. (1983) first used reverse-time migration for poststack or zero-offset data. The procedure underlying poststack reverse-time migration is the following: first, reverse the recorded data in time; second, use these reversed data as sources along the recording surface to propagate the wavefields in the subsurface; third, extract the image at zero time, e.g. apply an imaging condition. The principle of poststack reverse-time migration is that the subsurface reflectors work as exploding reflectors and that the wave equation used to propagate data can be applied either forward or backward in time by simply reversing the time axis (Levin, 1984).

Chang and McMechan (1986) apply reverse-time migration to prestack data. Prestack reverse-time migration reconstructs source and receiver wavefields. The source wavefield is reconstructed forward in time, and the receiver wavefield is reconstructed backward in time. Chang and McMechan (1986, 1994) use a so called excitation-time imaging condition, where images are formed by extracting the receiver wavefield at the time taken by a wave to travel from the source to the image point. This imaging condition is a special case of the cross-correlation imaging condition of Claerbout (1971).

## Elastic imaging vs. acoustic imaging

Multicomponent elastic data are often recorded in land or marine (ocean-bottom) seismic experiments. However, as mentioned earlier, elastic vector wavefields are not usually processed by specifically designed imaging procedures, but rather by extensions of techniques used for scalar wavefields. Thus, seismic data processing does not take full advantage of the information contained by elastic wavefields. In other words, it does not fully unravel reflections from complex geology or correctly preserve imaging amplitudes and estimate model parameters, etc.

Elastic wave propagation in a infinite homogeneous isotropic medium is charac-

terized by the wave equation (Aki and Richards, 2002)

$$\rho \frac{\partial^2 \mathbf{u}}{\partial t^2} = \mathbf{f} + (\lambda + 2\mu) \nabla (\nabla \cdot \mathbf{u}) - \mu \nabla \times \nabla \times \mathbf{u} \quad (1)$$

where  $\mathbf{u}$  is the vector displacement wavefield,  $t$  is time,  $\rho$  is the density,  $\mathbf{f}$  is the body source force,  $\lambda$  and  $\mu$  are the Lamé moduli. This wave equation assumes a slowly varying stiffness tensor over the imaging space. For isotropic media, one can process the elastic data either by separating wave-modes and migrating each mode using methods based on acoustic wave theory, or by migrating the whole elastic data set based on the elastic wave equation ???. The elastic wavefield extrapolation using equation ??? is usually performed in time by Kirchhoff migration or reverse-time migration.

Acoustic Kirchhoff migration is based on diffraction summation, which accumulates the data along diffraction curves in the data space and maps them onto the image space. For multicomponent elastic data, Kuo and Dai (1984a) discuss Kirchhoff migration for shot-record data. Here, identified PP and PS reflections can be migrated by computing source and receiver traveltimes using P-wave velocity for the source rays, and P- and S-wave velocities for the receiver rays. Hokstad (2000) performs multicomponent anisotropic Kirchhoff migration for multi-shot, multi-receiver experiments, where pure-mode and converted mode images are obtained by redatuming visco-elastic vector wavefields and application of a survey-sinking imaging condition to the reconstructed vector wavefields. The wavefield separation is effectively done by the Kirchhoff integral which handles both P- and S-waves, although this technique fails in areas of complex geology where ray theory breaks down.

Elastic reverse-time migration has the same two components as acoustic reverse-time migration: reconstruction of source and receiver wavefield and application of an imaging condition. The source and receiver wavefields are reconstructed by forward and backward propagation in time with various modeling approaches. For acoustic reverse-time migration, wavefield reconstruction is done with the acoustic wave-equation using the recorded scalar data as boundary condition. In contrast, for elastic reverse-time migration, wavefield reconstruction is done with the elastic wave-equation using the recorded vector data as boundary condition.

Since pure-mode and converted-mode reflections are mixed on all components of recorded data, images produced with reconstructed elastic wavefields are characterized by crosstalk due to the interference of various wave modes. In order to obtain images with clear physical meanings, most imaging conditions separate wave modes. There are two potential approaches to separate wavefields and image elastic seismic wavefields. The first option is to separate P and S modes on the acquisition surface from the recorded elastic wavefields. This procedure involves either approximations for the propagation path and polarization direction of the recorded data, or reconstruction of the seismic wavefields in the vicinity of the acquisition surface by a numerical solution of the elastic wave equation, followed by wavefield separation of scalar and vector potentials using Helmholtz decomposition (Etgen, 1988; Zhe

and Greenhalgh, 1997). An alternative data decomposition using P and S potentials reconstructs wavefields in the subsurface using the elastic wave equation, then decomposes the wavefields into P- and S-wave modes. This is followed by forward extrapolation of the separated wavefields back to the surface using the acoustic wave equation with the appropriate propagation velocity for the various wave modes (Sun et al., 2006) by conventional procedures used for scalar wavefields.

The second option is to extrapolate wavefields in the subsurface using a numerical solution to the elastic wave equation and then apply an imaging condition that extracts reflectivity information from the source and receiver wavefields. In the case where extrapolation is implemented by finite-difference methods (Chang and McMechan, 1986, 1994), this procedure is known as elastic reverse-time migration, and is conceptually similar to acoustic reverse-time migration (Baysal et al., 1983), which is more frequently used in seismic imaging.

Many imaging conditions can be used for reverse-time migration. Elastic imaging conditions are more complex than acoustic imaging conditions because both source and receiver wavefields are vector fields. Different elastic imaging conditions have been proposed for extracting reflectivity information from reconstructed elastic wavefields. Hokstad et al. (1998) use elastic reverse-time migration with Lamé potential methods. Chang and McMechan (1986) use the excitation-time imaging condition which extracts reflectivity information from extrapolated wavefields at traveltimes from the source to image positions computed by ray tracing, etc. Ultimately, these imaging conditions represent special cases of a more general type of imaging condition that involves time cross-correlation or deconvolution of source and receiver wavefields at every location in the subsurface.

## CONVENTIONAL ELASTIC IMAGING CONDITIONS

For vector elastic wavefields, the cross-correlation imaging condition needs to be implemented on all components of the displacement field. The problem with this type of imaging condition is that the source and receiver wavefields contain a mix of P- and S-wave modes which cross-correlate independently, thus hampering interpretation of migrated images. An alternative to this type of imaging performs wavefield separation of scalar and vector potentials after wavefield reconstruction in the imaging volume, but prior to the imaging condition and then cross-correlate pure modes from the source and receiver wavefields, as suggested by Dellinger and Etgen (1990) and illustrated by Cunha Filho (1992).

### Imaging with scalar wavefields

As mentioned earlier, assuming single scattering in the Earth (Born approximation), a conventional imaging procedure consists of two components: wavefield extrapolation and imaging. Wavefield extrapolation is used to reconstruct in the imaging

volume the seismic wavefield using the recorded data on the acquisition surface as a boundary condition, and imaging is used to extract reflectivity information from the extrapolated source and receiver wavefields.

Assuming scalar recorded data, wavefield extrapolation using a scalar wave equation reconstructs scalar source and receiver wavefields,  $u_s(\mathbf{x}, t)$  and  $u_r(\mathbf{x}, t)$ , at every location  $\mathbf{x}$  in the subsurface. Using the extrapolated scalar wavefields, a conventional imaging condition (?) can be implemented as cross-correlation at zero-lag time:

$$I(\mathbf{x}) = \int u_s(\mathbf{x}, t) u_r(\mathbf{x}, t) dt . \quad (2)$$

Here,  $I(\mathbf{x})$  denotes a scalar image obtained from scalar wavefields  $u_s(\mathbf{x}, t)$  and  $u_r(\mathbf{x}, t)$ ,  $\mathbf{x} = \{x, y, z\}$  represent Cartesian space coordinates, and  $t$  represents time.

## Imaging with vector displacements

Assuming vector recorded data, wavefield extrapolation using a vector wave equation reconstructs source and receiver wavefields  $\mathbf{u}_s(\mathbf{x}, t)$  and  $\mathbf{u}_r(\mathbf{x}, t)$  at every location  $\mathbf{x}$  in the subsurface. Here,  $\mathbf{u}_s$  and  $\mathbf{u}_r$  represent displacement fields reconstructed from data recorded by multicomponent geophones at the surface boundary. Using the vector extrapolated wavefields  $\mathbf{u}_s = \{u_{sx}, u_{sy}, u_{sz}\}$  and  $\mathbf{u}_r = \{u_{rx}, u_{ry}, u_{rz}\}$ , an imaging condition can be formulated as a straightforward extension of equation ?? by cross-correlating all combinations of components of the source and receiver wavefields. Such an imaging condition for vector displacements can be formulated mathematically as

$$I_{ij}(\mathbf{x}) = \int u_{si}(\mathbf{x}, t) u_{rj}(\mathbf{x}, t) dt , \quad (3)$$

where the quantities  $u_i$  and  $u_j$  stand for the Cartesian components  $x, y, z$  of the vector source and receiver wavefields,  $\mathbf{u}(\mathbf{x}, t)$ . For example,  $I_{zz}(\mathbf{x})$  represents the image component produced by cross-correlating of the  $z$  components of the source and receiver wavefields, and  $I_{zx}(\mathbf{x})$  represents the image component produced by cross-correlating of the  $z$  component of the source wavefield with the  $x$  component of the receiver wavefield, etc. In general, an image produced with this procedure has nine components at every location in space.

The main drawback of applying this type of imaging condition is that the wavefield used for imaging contains a combination of P- and S-wave modes. Those wavefield vectors interfere with one-another in the imaging condition, since the P and S components are not separated in the extrapolated wavefields. The crosstalk between various components of the wavefield creates artifacts and makes it difficult to interpret the images in terms of pure wave modes, e.g. PP or PS reflections. This situation is similar to the case of imaging with acoustic data contaminated by multiples or other types of coherent noise which are mapped in the subsurface using an incorrect velocity.

## Imaging with scalar and vector potentials

An alternative to the elastic imaging condition from equation ?? is to separate the extrapolated wavefield into P and S potentials after extrapolation and image using cross-correlations of the vector and scalar potentials (Dellinger and Etgen, 1990). Separation of scalar and vector potentials can be achieved by Helmholtz decomposition, which is applicable to any vector field  $\mathbf{u}(\mathbf{x}, t)$ :

$$\mathbf{u} = \nabla\Phi + \nabla \times \boldsymbol{\Psi} , \quad (4)$$

where  $\Phi(\mathbf{x}, t)$  represents the scalar potential of the wavefield  $\mathbf{u}(\mathbf{x}, t)$  and  $\boldsymbol{\Psi}(\mathbf{x}, t)$  represents the vector potential of the wavefield  $\mathbf{u}(\mathbf{x}, t)$ , and  $\nabla \cdot \boldsymbol{\Psi} = 0$ . For isotropic elastic wavefields, equation ?? is not used directly in practice, but the scalar and vector components are obtained indirectly by the application of the divergence ( $\nabla \cdot$ ) and curl ( $\nabla \times$ ) operators to the extrapolated elastic wavefield  $\mathbf{u}(\mathbf{x}, t)$ :

$$P = \nabla \cdot \mathbf{u} = \nabla^2 \Phi , \quad (5)$$

$$\mathbf{S} = \nabla \times \mathbf{u} = -\nabla^2 \boldsymbol{\Psi} . \quad (6)$$

For isotropic elastic fields far from the source, quantities  $P$  and  $\mathbf{S}$  describe compressional and transverse components of the wavefield, respectively (Aki and Richards, 2002). In 2D, the quantity  $\mathbf{S}$  corresponds to SV waves that are polarized in the propagation plane.

Using the separated scalar and vector components, we can formulate an imaging condition that combines various incident and reflected wave modes. The imaging condition for vector potentials can be formulated mathematically as

$$I_{ij}(\mathbf{x}) = \int \alpha_{si}(\mathbf{x}, t) \alpha_{rj}(\mathbf{x}, t) dt , \quad (7)$$

where the quantities  $\alpha_i$  and  $\alpha_j$  stand for the various wave modes  $\alpha = \{P, S\}$  of the vector source and receiver wavefields  $\mathbf{u}(\mathbf{x}, t)$ . For example,  $I_{PP}(\mathbf{x})$  represents the image component produced by cross-correlating of the  $P$  wave mode of the source and receiver wavefields, and  $I_{PS}(\mathbf{x})$  represents the image component produced by cross-correlating of the  $P$  wave mode of the source wavefield with the  $S$  wave-mode of the receiver wavefield, etc. In isotropic media, an image produced with this procedure has four independent components at every location in space, similar to the image produced by the cross-correlation of the various Cartesian components of the vector displacements. However, in this case, the images correspond to various combinations of incident P or S and reflected P- or S-waves, thus having clear physical meaning and being easier to interpret for physical properties.

## EXTENDED ELASTIC IMAGING CONDITIONS

The conventional imaging condition from equation ?? discussed in the preceding section uses zero space- and time-lags of the cross-correlation between the source and receiver wavefields. This imaging condition represents a special case of a more general form of an extended imaging condition (Sava and Fomel, 2006b)

$$I(\mathbf{x}, \boldsymbol{\lambda}, \tau) = \int u_s(\mathbf{x} - \boldsymbol{\lambda}, t - \tau) u_r(\mathbf{x} + \boldsymbol{\lambda}, t + \tau) dt, \quad (8)$$

where  $\boldsymbol{\lambda} = \{\lambda_x, \lambda_y, \lambda_z\}$  and  $\mathbf{t}$  stand for cross-correlation lags in space and time, respectively. The imaging condition from equation ?? is equivalent to the extended imaging condition from equation ?? for  $\boldsymbol{\lambda} = \mathbf{0}$  and  $\mathbf{t} = 0$ .

The extended imaging condition has two main uses. First, it characterizes wavefield reconstruction errors, since for incorrectly reconstructed wavefields, the cross-correlation energy does not focus completely at zero lags in space and time. Sources of wavefield reconstruction errors include inaccurate numeric solutions to the wave-equation, inaccurate models used for wavefield reconstruction, inadequate wavefield sampling on the acquisition surface, and uneven illumination of the subsurface. Typically, all these causes of inaccurate wavefield reconstruction occur simultaneously and it is difficult to separate them after imaging. Second, assuming accurate wavefield reconstruction, the extended imaging condition can be used for angle decomposition. This leads to representations of reflectivity as a function of angles of incidence and reflection at all points in the imaged volume (Sava and Fomel, 2003). Here, we assume that wavefield reconstruction is accurate and concentrate on further extensions of the imaging condition, such as angle decomposition.

### Imaging with vector displacements

For imaging with vector wavefields, the extended imaging condition from equation ?? can be applied directly to the various components of the reconstructed source and receiver wavefields, similar to the conventional imaging procedure described in the preceding section. Therefore, an extended image constructed from vector displacement wavefields is

$$I_{ij}(\mathbf{x}, \boldsymbol{\lambda}, \tau) = \int u_{si}(\mathbf{x} - \boldsymbol{\lambda}, t - \tau) u_{rj}(\mathbf{x} + \boldsymbol{\lambda}, t + \tau) dt, \quad (9)$$

where the quantities  $u_{si}$  and  $u_{rj}$  stand for the Cartesian components  $x, y, z$  of the vector source and receiver wavefields, and  $\boldsymbol{\lambda}$  and  $\mathbf{t}$  stand for cross-correlation lags in space and time, respectively. This imaging condition suffers from the same drawbacks described for the similar conventional imaging condition applied to the Cartesian components of the reconstructed wavefields, i.e. crosstalk between the unseparated wave modes.

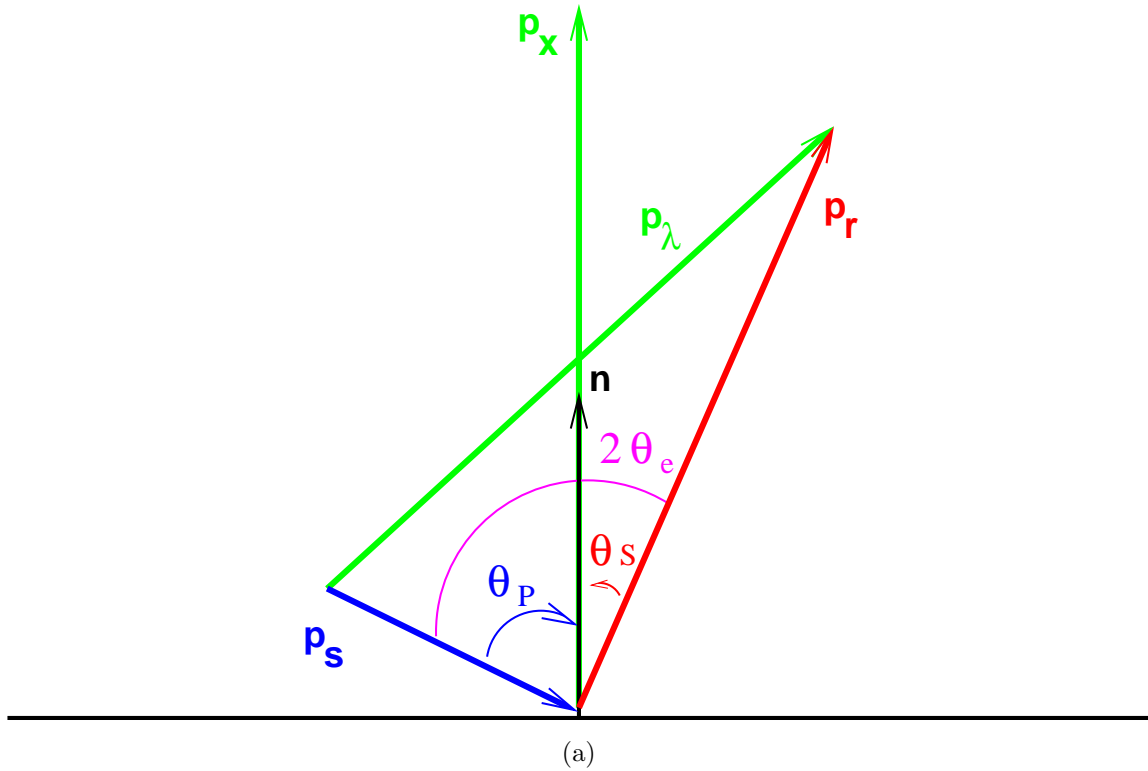


Figure 1: Local wave vectors of the converted wave at a common image point location in 3D. The plot shows the conversion in the reflection plane in 2D.  $\mathbf{p}_s$ ,  $\mathbf{p}_r$ ,  $\mathbf{p}_x$  and  $\mathbf{p}_\lambda$  are ray parameter vectors for the source ray, receiver ray, and combinations of the two. The length of the incidence and reflection wave vectors are inversely proportional to the incidence and reflection wave velocity, respectively. Vector  $\mathbf{n}$  is the normal of the reflector. By definition,  $\mathbf{p}_x = \mathbf{p}_r - \mathbf{p}_s$  and  $\mathbf{p}_\lambda = \mathbf{p}_r + \mathbf{p}_s$ .

## Imaging with scalar and vector potentials

An extended imaging condition can also be designed for elastic wavefields decomposed in scalar and vector potentials, similar to the conventional imaging procedure described in the preceding section. Therefore, an extended image constructed from scalar and vector potentials is

$$I_{ij}(\mathbf{x}, \boldsymbol{\lambda}, \tau) = \int \alpha_{si}(\mathbf{x} - \boldsymbol{\lambda}, t - \tau) \alpha_{rj}(\mathbf{x} + \boldsymbol{\lambda}, t + \tau) dt, \quad (10)$$

where the quantities  $\alpha_{si}$  and  $\alpha_{rj}$  stand for the various wave modes  $\alpha = \{P, S\}$  of the source and receiver wavefields, and  $\boldsymbol{\lambda}$  and  $\mathbf{t}$  stand for cross-correlation lags in space and time, respectively.

### ANGLE DECOMPOSITION

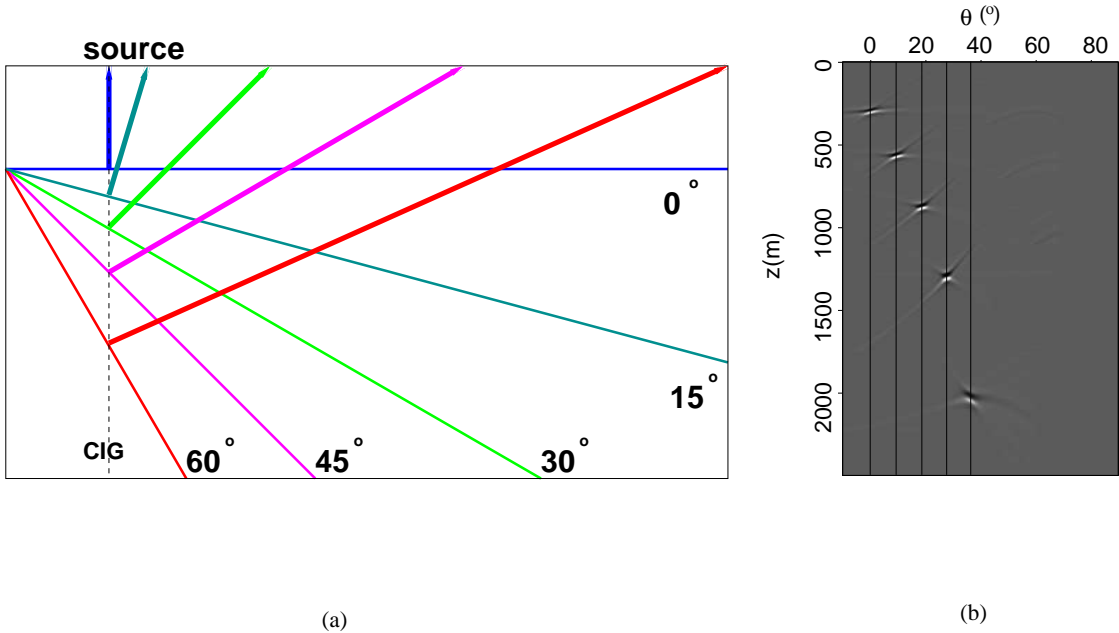


Figure 2: (a) Model showing one shot over multiple reflectors dipping at  $0^\circ$ ,  $15^\circ$ ,  $30^\circ$ ,  $45^\circ$  and  $60^\circ$ . The vertical dashed line shows a CIG location. Incidence ray is vertically down and P to S conversions are marked by arrowed lines pointing away from reflectors. (b) Converted wave angle gather obtained from algorithm described by Sava and Fomel (2006a). Notice that converted wave angles are always smaller than incidence angles (in this case, the dips of the reflectors) except for normal incidence.

As indicated earlier, the main uses of images constructed using extended imaging conditions are migration velocity analysis (MVA) and amplitude versus angle analysis (AVA). Such analyses, however, require that the images be decomposed in components corresponding to various angles of incidence. Angle decomposition takes

different forms corresponding to the type of wavefields involved in imaging. Thus, we can distinguish angle decomposition for scalar (acoustic) wavefields and angle decomposition for vector (elastic) wavefields.

## Scalar wavefields

For the case of imaging with the acoustic wave equation, the reflection angle corresponding to incidence and reflection of P-wave mode can be constructed after imaging, using mapping based on the relation (Sava and Fomel, 2005)

$$\tan \theta_a = \frac{|\mathbf{k}_\lambda|}{|\mathbf{k}_x|}, \quad (11)$$

where  $\theta_a$  is the incidence angle, and  $\mathbf{k}_x = \mathbf{k}_r - \mathbf{k}_s$  and  $\mathbf{k}_\lambda = \mathbf{k}_r + \mathbf{k}_s$  are defined using the source and receiver wavenumbers,  $\mathbf{k}_s$  and  $\mathbf{k}_r$ . The information required for decomposition of the reconstructed wavefields as a function of wavenumbers  $\mathbf{k}_x$  and  $\mathbf{k}_\lambda$  is readily available in the images  $I(\mathbf{x}, \boldsymbol{\lambda}, \tau)$  constructed by extended imaging conditions equations ?? or ?. After angle decomposition, the image  $I(\mathbf{x}, \theta, \phi)$  represents a mapping of the image  $I(\mathbf{x}, \boldsymbol{\lambda}, \tau)$  from offsets to angles. In other words, all information for characterizing angle-dependent reflectivity is already available in the image obtained by the extended imaging conditions.

## Vector wavefields

A similar approach can be used for decomposition of the reflectivity as a function of incidence and reflection angles for elastic wavefields imaged with extended imaging conditions equations ?? or ?. The angle  $\theta_e$  characterizing the average angle between incidence and reflected rays can be computed using the expression (Sava and Fomel, 2005)

$$\tan^2 \theta_e = \frac{(1 + \gamma)^2 |\mathbf{k}_\lambda|^2 - (1 - \gamma)^2 |\mathbf{k}_x|^2}{(1 + \gamma)^2 |\mathbf{k}_x|^2 - (1 - \gamma)^2 |\mathbf{k}_\lambda|^2}, \quad (12)$$

where  $\gamma$  is the velocity ratio of the incident and reflected waves, e.g.  $V_P/V_S$  ratio for incident P mode and reflected S mode. Figure 1 shows the schematic and the notations used in equation ??, where  $|\mathbf{p}_x| = |\mathbf{k}_x|/\omega$ ,  $|\mathbf{p}_\lambda| = |\mathbf{k}_\lambda|/\omega$ , and  $\omega$  is the angular frequency at the imaging location  $\mathbf{x}$ . The angle decomposition equation ?? is designed for PS reflections and reduces to equation ?? for PP reflections when  $\gamma = 1$ .

Angle decomposition using equation ?? requires computation of an extended imaging condition with 3D space lags  $(\lambda_x, \lambda_y, \lambda_z)$ , which is computationally costly. Faster computation can be done if we avoid computing the vertical lag  $\lambda_z$ , in which case the

angle decomposition can be done using the expression (Sava and Fomel, 2005):

$$\tan \theta_e = \frac{(1 + \gamma)(a_{\lambda_x} + b_x)}{2\gamma k_z + \sqrt{4\gamma^2 k_z^2 + (\gamma^2 - 1)(a_{\lambda_x} + b_x)(a_x + b_{\lambda_x})}}, \quad (13)$$

where  $a_{\lambda_x} = (1 + \gamma)k_{\lambda_x}$ ,  $a_x = (1 + \gamma)k_x$ ,  $b_{\lambda_x} = (1 - \gamma)k_{\lambda_x}$ , and  $b_x = (1 - \gamma)k_x$ . Figure 2 shows a model of five reflectors and the extracted angle gathers for these reflectors at the location of the source. For PP reflections, they would occur in the angle gather at angles equal with the reflector slopes. However, for PS reflections, as illustrated in Figure 2, the reflection angles are smaller than the reflector slopes, as expected.

## EXAMPLES

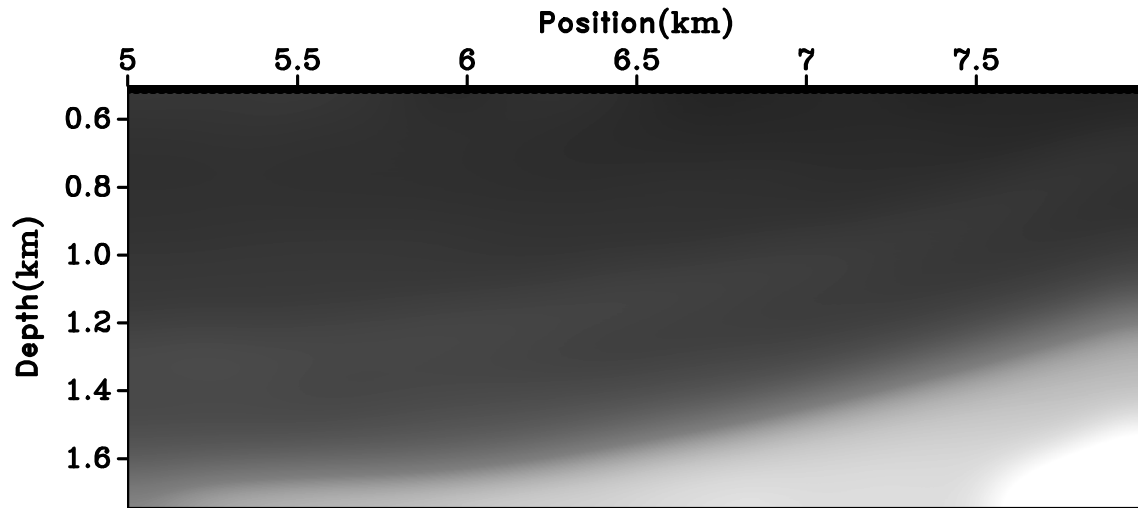
We test the different imaging conditions discussed in the preceding sections with data simulated on a modified subset of the Marmousi II model (Martin et al., 2002). The section is chosen to be at the left side of the entire model which is relatively simple, and therefore it is easier to examine the quality of the images.

### Imaging with vector displacements

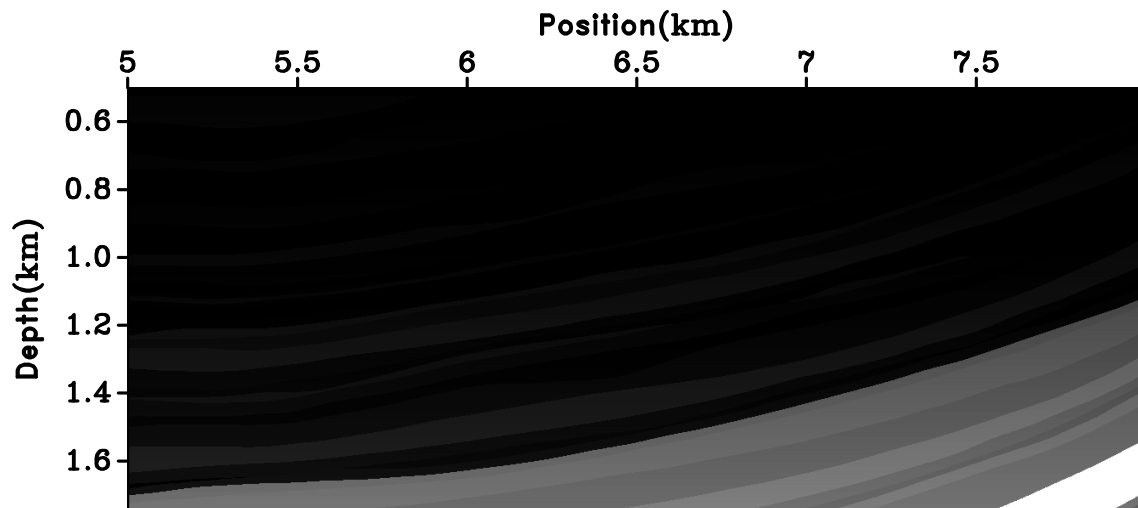
Consider the images obtained for the model depicted in Figures 3(a) and 3(b). Figure 3(a) depicts the P-wave velocity (smooth function between 1.6 – 3.2 km/s), and Figure 3(b) shows the density (variable between 1 – 2 g/cm<sup>3</sup>). The S-wave velocity is a scaled version of the P-wave velocity with  $V_P/V_S = 2$ . We use a smooth velocity background for both modeling and migration. We use density discontinuities to generate reflections in modeling, but use a constant density in migration. The smooth velocity background for both modeling and migration is used to avoid back-scattering during wavefield reconstruction. The elastic data, Figures 4(a) and 4(b), are simulated using a space-time staggered-grid finite-difference solution to the isotropic elastic wave equation (Virieux, 1984, 1986; Mora, 1987, 1988). We simulate data for a source located at position  $x = 6.75$  km and  $z = 0.5$  km. Since we are using an explosive source and the background velocity is smooth, the simulated wavefield is represented mainly by P-wave incident energy and the receiver wavefield is represented by a combination of P- and S-wave reflected energy. The data contain a mix of P and S modes, as can be seen by comparing the vertical and horizontal displacement components, shown in Figures 4(a) and 4(b), with the separated P and S wave modes, shown in Figures 4(c) and 4(d).

Imaging the data shown in Figures 4(a) and 4(b) using the imaging condition from equation ??, we obtain the images depicted in Figures 5(a) to 5(d). Figures 5(a) to 5(d) correspond to the cross-correlation of the  $z$  and  $x$  components of the source wavefield with the  $z$  and  $x$  components of the receiver wavefield, respectively. Since the input data do not represent separated wave modes, the images produced with the

imaging condition based on vector displacements do not separate PP and PS reflectivity. Thus, the images are hard to interpret, since it is not clear what incident and reflected wave modes the reflections represent. In reality, reflections corresponding to all wave modes are present in all panels.



(a)



(b)

Figure 3: (a) P- and S-wave velocity models and (b) density model used for isotropic elastic wavefield modeling, where  $V_P$  ranges from 1.6 to 3.2 km/s from top to bottom and  $V_P/V_S = 2$ , and density ranges from 1 to 2 g/cm<sup>3</sup>.

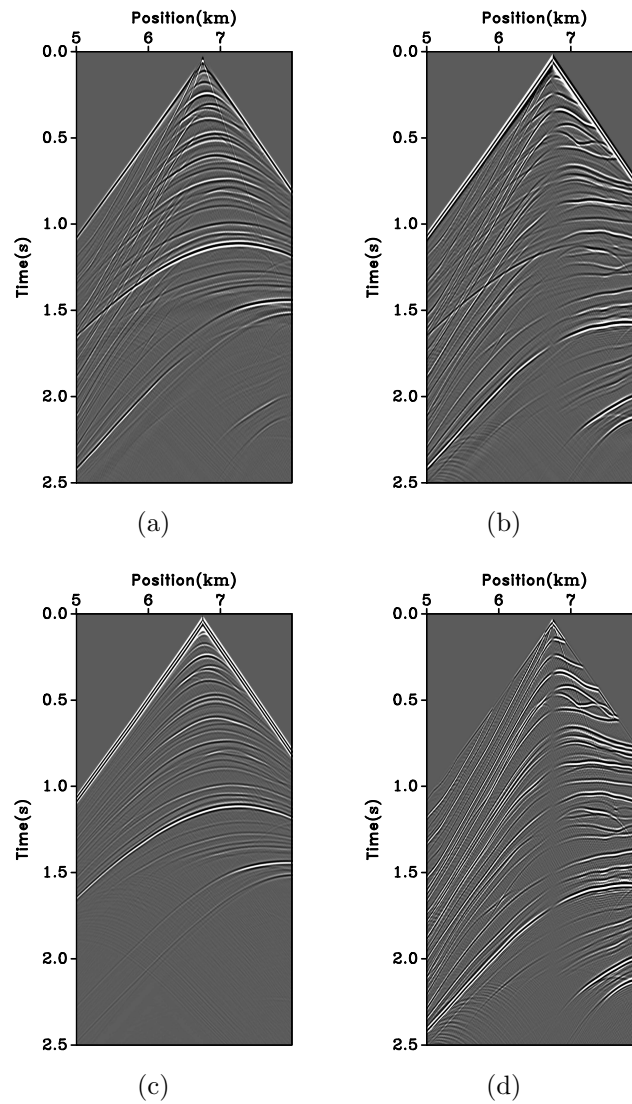


Figure 4: Elastic data simulated in model 3(a) and 3(b) with a source at  $x = 6.75$  km and  $z = 0.5$  km, and receivers at  $z = 0.5$  km: (a) vertical component, (b) horizontal component, (c) scalar potential and (d) vector potential of the elastic wavefield. Both vertical and horizontal components, panels (a) and (b), contain a mix of P and S modes, as seen by comparison with panels (c) and (d).

## Imaging with scalar and vector potentials

Consider the images (Figures 6) obtained using the imaging condition from equation ?? applied to the data (Figures 4(a) and 4(b)) from the preceding example. Because we used an explosive source for our simulation, the source wavefield contains mostly P-wave energy, while the receiver wavefield contains P- and S-wave mode energy. Helmholtz decomposition after extrapolation but prior to imaging isolates P and S wavefield components. Therefore, migration produces images of reflectivity corresponding to PP and PS reflections, Figures 6(a) and 6(b), but not reflectivity corresponding to SP or SS reflections, Figures 6(c) and 6(d). The illumination regions are different between PP and PS images, due to different illumination angles of the two propagation modes for the given acquisition geometry. The PS image, Figure 6(b), also shows the usual polarity reversal for positive and negative angles of incidence measured relative to the reflector normal. By comparing Figures 6(a) and 6(b) with Figures 5(a) and 5(b), it is apparent that the crosstalk in the images obtained from displacement-based imaging condition is more prominent than the one obtained from potential-based imaging conditions, especially in Figure 5(a). Furthermore, the polarity in Figure 5(b), normally taken as the PS image, does not reverse polarity at normal incidence, which is not correct either.

## Angle decomposition

The images shown in the preceding subsection correspond to the conventional imaging conditions from equations ?? and ?. We can construct other images using the extended imaging conditions from equations ?? and ?, which can be used for angle decomposition after imaging. Then, we can use equation ?? to compute angle gathers from horizontal space cross-correlation lags.

Figures ?? and ?? together with Figures ?? and ?? show, respectively, the PP and PS horizontal lags and angle gathers for the common image gather (CIG) location in the middle of the reflectivity model, given a single source at  $x = 6.75$  km and  $z = 0.5$  km. PP and PS horizontal lags are lines dipping at angles that are equal to the incidence angles (real incidence angles for PP reflection and average of incidence and reflection angles for PS reflection) at the CIG location. PP angles are larger than PS angles at all reflectors, as illustrated on the simple synthetic example shown in Figure 2.

Figures 8(a) and 8(c) together with Figures 8(b) and 8(d) show, respectively, the PP and PS horizontal lags and angle gathers for the same CIG location, given many sources from  $x = 5.5$  to  $7.5$  km and  $z = 0.5$  km. The horizontal space cross-correlation lags are focused around  $\boldsymbol{\lambda} = \mathbf{0}$ , which justifies the use of conventional imaging condition extracting the cross-correlation of the source and receiver wavefields at zero lag in space and time. Thus, the zero lag of the images obtained by extended imaging condition represent the image at the particular CIG location. The PP and PS gathers for many sources are flat, since the migration was done with correct migration

velocity. The PS angle gather, depicted in Figure 8(d), shows a polarity reversal at  $\theta = 0$  as expected.

## DISCUSSION

Our presentation of the angle-domain reverse-time migration method outlined in the preceding sections deliberately ignores several practical challenges in order to maintain the focus of this paper to the actual elastic imaging condition. However, for completeness, we would like to briefly mention several complementary issues that need to be addressed in conjunction with the imaging condition in order to design a practical method for elastic reverse-time migration.

First, reconstruction of the receiver wavefield requires that the multicomponent recorded data be injected into the model in reverse-time. In other words, the recorded data act as a displacement sources at receiver positions. In elastic materials, displacement sources trigger both compressional and transverse wave modes, no matter what portion of the recorded elastic wavefield is used as a source. For example, injecting a recorded compressional mode triggers both a compressional (physical) mode and a transverse (non-physical) mode in the subsurface. Both modes propagate in the subsurface and might correlate with wave modes from the source side. There are several ways to address this problem, such as by imaging in the angle-domain where the non-physical modes appear as events with non-flat moveout. We can make an analogy between those non-physical waves and multiples that also lead to non-flat events in the angle-domain. Thus, the source injection artifacts might be eliminated by filtering the migrated images in the angle domain, similar to the technique employed by Sava and Guitton (2005) for suppressing multiples after imaging.

Second, the data recorded at a free surface contain both up-going and down-going waves. Ideally, we should use only the up-going waves as a source for reconstructing the elastic wavefields by time-reversal. In our examples, we assume an absorbing surface in order to avoid this additional complication and concentrate on the imaging condition. However, practical implementations require directional separation of waves at the surface (Wapenaar and Haimé, 1990; Wapenaar et al., 1990; Admundsen and Reitan, 1995; Admundsen et al., 2001; Hou and Marfurt, 2002). Furthermore, a free surface allows other wave modes to be generated in the process of wavefield reconstruction using the elastic wave-equation, e.g. Rayleigh and Love waves. Although those waves do not propagate deep into the model, they might interfere with the directional wavefield separation at the surface.

Third, we suggest in this paper that angle-dependent reflectivity constructed using extended imaging conditions might allow for elastic AVA analysis. This theoretical possibility requires that the wavefields are correctly reconstructed in the subsurface to account for accurate amplitude variation. For example, boundaries between regions with different material properties need to be reasonably located in the subsurface to generate correct mode conversions, and the radiation pattern of the source also needs

to be known. Neither one of these aspects is part of our analyses, but they represent important considerations for practical elastic wavefield imaging.

Fourth, the wave-mode separation using divergence and curl operators, as required by Helmholtz decomposition, does not work well in elastic anisotropic media. Anisotropy requires that the separation operators take into account the local anisotropic parameters that may vary spatially (?). However, we do not discuss anisotropic wave-mode decomposition in this paper and restrict our attention to angle-domain imaging in isotropic models.

## CONCLUSIONS

We present a method for reverse-time migration with angle-domain imaging formulated for multicomponent elastic data. The method is based on the separation of elastic wavefields reconstructed in the subsurface into pure wave-modes using conventional Helmholtz decomposition. Elastic wavefields from the source and receivers are separated into pure compressional and transverse wave-modes which are then used for angle-domain imaging. The images formed using this procedure are interpretable in terms of the subsurface physical properties, for example, by analyzing the PP or PS angle-dependent reflectivity. In contrast, images formed by simple cross-correlation of Cartesian components of reconstructed elastic wavefields mix contributions from P and S reflections and are harder to interpret. Artifacts caused by back-propagating the recorded data with displacement sources are present in both types of images, although they are easier to distinguish and attenuate on the images constructed with pure elastic wave-modes separated prior to imaging.

The methodology is advantageous not only because it forms images with clearer physical meaning, but also because it is based on more accurate physics of wave propagation in elastic materials. For example, this methodology allows for wave-mode conversions in the process of wavefield reconstruction. This is in contrast with alternative methods for multicomponent imaging which separate wave-modes on the surface and then image those independently. In addition, elastic images can be formed in the angle-domain using extended imaging conditions, which offers the potential for migration velocity analysis (MVA) and amplitude versus angle (AVA) analysis.

## ACKNOWLEDGMENT

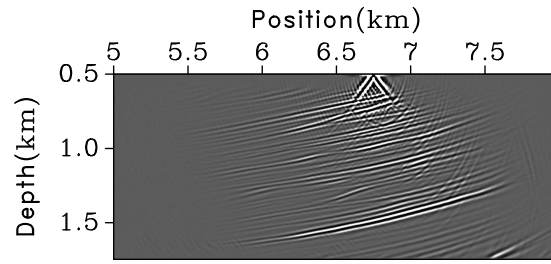
We acknowledge the support of the sponsors of the Center for Wave Phenomena at Colorado School of Mines. We also acknowledge Geophysics Associate Editor John Etgen and reviewers Dan Whitmore, Jim Gaiser and Paul Fowler whose comments and suggestions have significantly improved the manuscript.

## REFERENCES

- Admundsen, L., L. Ikelle, and L. Berg, 2001, Multidimensional signature deconvolution and free surface multiple elimination of marine multicomponent ocean-bottom seismic data: *Geophysics*, **66**, 1594–1604.
- Admundsen, L., and A. Reitan, 1995, Decomposition of multicomponent sea-floor data into upgoing and downgoing P and S waves: *Geophysics*, **60**, 560–572.
- Aki, K., and P. Richards, 2002, *Quantitative seismology* (second edition): University Science Books.
- Alford, R. M., K. R. Kelly, and D. M. Boore, 1974, Accuracy of finite-difference modeling of the acoustic wave equation: *Geophysics*, **39**, 834–842.
- Baysal, E., D. D. Kosloff, and J. W. C. Sherwood, 1983, Reverse time migration: *Geophysics*, **48**, 1514–1524.
- Boechat, J. B., A. B., D. M. S. Filho, P. M. Cunha, W. J. Mansur, and T. Moreira, 2007, A 3D reverse-time migration scheme for offshore seismic data: *SEG Technical Program Expanded Abstracts*, **26**, 2427–2431.
- Bolt, B. A., and W. D. Smith, 1976, Finite-element computation of seismic anomalies for bodies of arbitrary shape (short note): *Geophysics*, **41**, 145–151.
- Chang, W. F., and G. A. McMechan, 1986, Reverse-time migration of offset vertical seismic profiling data using the excitation-time imaging condition: *Geophysics*, **51**, 67–84.
- , 1994, 3-D elastic prestack, reverse-time depth migration: *Geophysics*, **59**, 597–609.
- Claerbout, J. F., 1971, Toward a unified theory of reflector mapping: *Geophysics*, **36**, 467–481.
- Clayton, R. W., 1981, *Wavefield inversion methods for refraction and reflection data*: PhD thesis, Stanford University.
- Clayton, R. W., and D. Brown, 1979, The choice of variables for elastic wave extrapolation: *SEP-Report*, **20**, 73–96.
- Cunha Filho, C., 1992, *Elastic modeling and migration in earth models*: PhD thesis, Stanford University.
- Dablain, M. A., 1986, The application of high-order differencing to the scalar wave equation: *Geophysics*, **51**, 54–66.
- Dai, N., and S. Cheadle, 1996, Pseudo-spectral migration in the f-x domain: *SEG Technical Program Expanded Abstracts*, **15**, 427–430.
- Dellinger, J., and J. Etgen, 1990, Wave-field separation in two-dimensional anisotropic media (short note): *Geophysics*, **55**, 914–919.
- Etgen, J. T., 1988, Prestacked migration of P and SV-waves: *SEG Technical Program Expanded Abstracts*, **7**, 972–975.
- Fomel, S., and M. M. Backus, 2003, Multicomponent seismic data registration by least squares: *SEG Technical Program Expanded Abstracts*, **22**, 781–784.
- Gaiser, J., 1996, Multicomponent  $V_p/V_s$  correlation analysis: *Geophysics*, **61**, 1137–1149.
- Gaiser, J., N. Moldoveanu, C. Macbeth, R. Michelena, and S. Spitz, 2001, Multicomponent technology: the players, problems, applications, and trends: Summary of

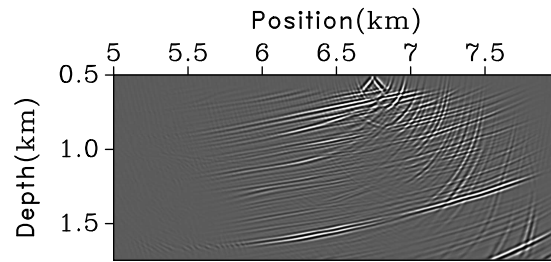
- the workshop sessions: The Leading Edge, **20**, 974–977.
- Gray, S. H., J. Etgen, J. Dellinger, and D. Whitmore, 2001, Seismic migration problems and solutions: *Geophysics*, **66**, 1622–1640.
- Hokstad, K., 2000, Multicomponent Kirchhoff migration: *Geophysics*, **65**, 861–873.
- Hokstad, K., R. Mittet, and M. Landro, 1998, Elastic reverse time migration of marine walkaway vertical seismic profiling data: *Geophysics*, **63**, 1685–1695.
- Hou, A., and K. Marfurt, 2002, Multicomponent prestack depth migration by scalar wavefield extrapolation: *Geophysics*, **67**, 1886–1894.
- Jones, I. F., M. C. Goodwin, I. D. Berranger, H. Zhou, and P. A. Farmer, 2007, Application of anisotropic 3D reverse time migration to complex North Sea imaging: SEG Technical Program Expanded Abstracts, **26**, 2140–2144.
- Knapp, S., N. Payne, and T. Johns, 2001, Imaging through gas clouds: A case history from the gulf of mexico: SEG Technical Program Expanded Abstracts, **20**, 776–779.
- Kuo, J. T., and T. F. Dai, 1984a, Kirchhoff elastic wave migration for the case of noncoincident source and receiver: *Geophysics*, **49**, 1223–1238.
- , 1984b, Kirchhoff elastic wave migration for the case of noncoincident source and receiver: *Geophysics*, **49**, 1223–1238. (Discussion in GEO-50-05-0872-0872; Reply in GEO-50-05-0872-0872).
- Levin, S. A., 1984, Principle of reverse-time migration: *Geophysics*, **49**, 581–583.
- Li, X. Y., 1998, Fracture detection using P-P and P-S waves in multicomponent sea-floor data: SEG Technical Program Expanded Abstracts, **17**, 2056–2059.
- Martin, G. S., K. J. Marfurt, and S. Larsen, 2002, Marmousi-2: An updated model for the investigation of avo in structurally complex areas: SEG Technical Program Expanded Abstracts, **21**, 1979–1982.
- McMechan, G. A., 1982, Determination of source parameters by wavefield extrapolation: *Geophysical Journal International*, **71**, 613–628.
- , 1983, Migration by extrapolation of time-dependent boundary values: *Geophysical Prospecting*, **31**, 413–420.
- Mora, P., 1988, Elastic wave-field inversion of reflection and transmission data: *Geophysics*, **53**, 750–759.
- Mora, P. R., 1987, Nonlinear two-dimensional elastic inversion of multioffset seismic data: *Geophysics*, **52**, 1211–1228.
- Nickel, M., and L. Sonneland, 2004, Automated PS to PP event registration and estimation of a high-resolution Vp-Vs ratio volume: SEG Technical Program Expanded Abstracts, **23**, 869–872.
- Pestana, R. C., F. M. R. da Mota, T. J. Ulrych, S. Freire, and F. B. da Silva, 1989, Deterministic and stochastic separation of P and SV-waves: A comparison: SEG Technical Program Expanded Abstracts, **8**, 1308–1311.
- Sava, P., and S. Fomel, 2003, Angle-domain common image gathers by wavefield continuation methods: *Geophysics*, **68**, 1065–1074.
- , 2005, Wave-equation common-angle gathers for converted waves: SEG Technical Program Expanded Abstracts, **24**, 947–950.
- , 2006a, Time-shift imaging condition for converted waves: SEG Technical Program Expanded Abstracts, **25**, 2460–2464.
- , 2006b, Time-shift imaging condition in seismic migration: *Geophysics*, **71**,

- S209–S217.
- Sava, P., and A. Guitton, 2005, Multiple attenuation in the image space: *Geophysics*, **70**, V10–V20.
- Seriani, G., and E. Priolo, 1991, High-order spectral element method for acoustic wave modeling: *SEG Technical Program Expanded Abstracts*, **10**, 1561–1564.
- Seriani, G., E. Priolo, J. Carcione, and E. Padovani, 1992, High-order spectral element method for elastic wave modeling: *SEG Technical Program Expanded Abstracts*, **11**, 1285–1288.
- Simmons, J., and M. Backus, 2003, An introduction—Multicomponent: *The Leading Edge*, **22**, 1227–1262.
- Stewart, R. R., J. E. Gaiser, R. J. Brown, and D. C. Lawton, 2003, Converted-wave seismic exploration: Applications: *Geophysics*, **68**, 40–57.
- Sun, R., G. A. McMechan, C. S. Lee, J. Chow, and C. H. Chen, 2006, Prestack scalar reverse-time depth migration of 3D elastic seismic data: *Geophysics*, **71**, S199–S207.
- Virieux, J., 1984, SH-wave propagation in heterogeneous media - Velocity-stress finite-difference method: *Geophysics*, **49**, 1933–1942.
- , 1986, P-SV wave propagation in heterogeneous media - Velocity-stress finite-difference method: *Geophysics*, **51**, 889–901.
- Wapenaar, C. P. A., and G. C. Haimé, 1990, Elastic extrapolation of seismic P- and S-waves: *Geophysical Prospecting*, **38**, 23–60.
- Wapenaar, C. P. A., P. Herrmann, D. J. Verschuur, and A. J. Berkhout, 1990, Decomposition of multicomponent seismic data into primary P- and S-wave responses: *Geophysical Prospecting*, **38**, 633–661.
- Wapenaar, C. P. A., N. A. Kinneging, and A. J. Berkhout, 1987, Principle of prestack migration based on the full elastic two-way wave equation: *Geophysics*, **52**, 151–173.
- Whitmore, N. D., 1983, Iterative depth migration by backward time propagation: *SEG Technical Program Expanded Abstracts*, **2**, 382–385.
- , 1995, An imaging hierarchy for common-angle seismograms: PhD thesis, The University of Tulsa.
- Zhe, J., and S. A. Greenhalgh, 1997, Prestack multicomponent migration: *Geophysics*, **62**, 598–613.
- Zhu, X., S. Altan, and J. Li, 1999, Recent advances in multicomponent processing: *The Leading Edge*, **18**, 1283–1288.



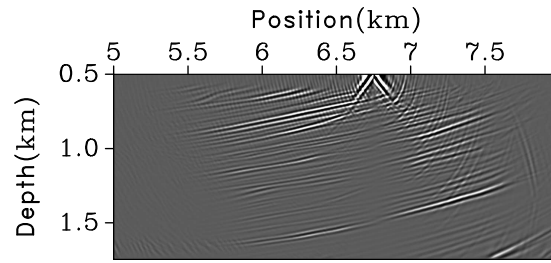
pp

(a)



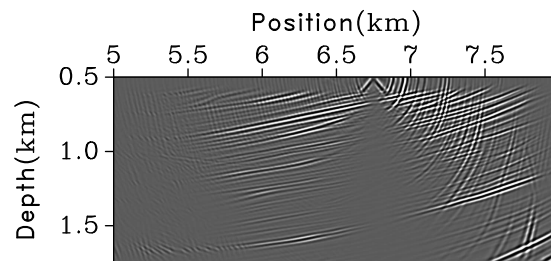
ps

(b)



sp

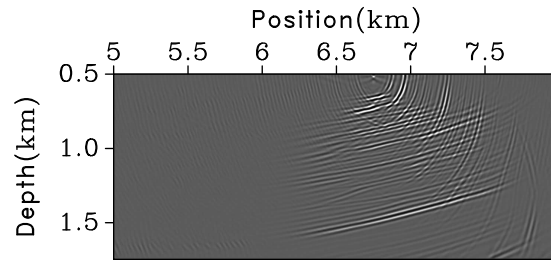
(c)



ss

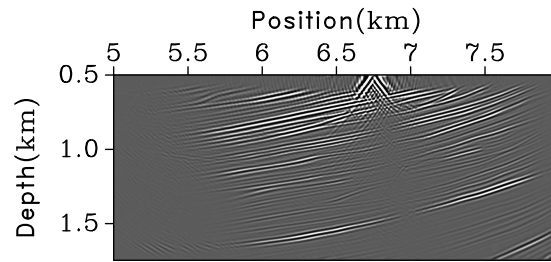
(d)

Figure 5: Images produced with the displacement components imaging condition from equation ???. Panels (a), (b), (c) and (d) correspond to the cross-correlation of the vertical and horizontal components of the source wavefield with the vertical and horizontal components of the receiver wavefield, respectively. Images (a) to (d) are the  $zz$ ,  $zx$ ,  $xz$  and  $xx$  components, respectively. The image corresponds to one shot at position  $x = 6.75$  km and  $z = 0.5$  km. Receivers are located at all locations at  $z = 0.5$  km.



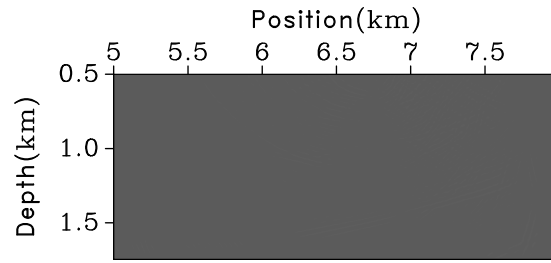
pp

(a)



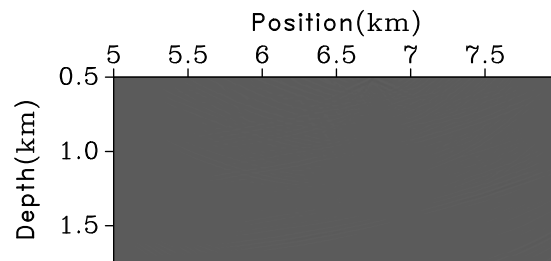
ps

(b)



sp

(c)



ss

(d)

Figure 6: Images produced with the scalar and vector potentials imaging condition from equation ???. Panels (a), (b), (c) and (d) correspond to the cross-correlation of the P and S components of the source wavefield with the P and S components of the receiver wavefield, respectively. Images (a) to (d) are the  $PP$ ,  $PS$ ,  $SP$  and  $SS$  components, respectively. The image corresponds to one shot at position  $x = 6.75$  km and  $z = 0.5$  km. Receivers are located at all locations at  $z = 0.5$  km. Panels (c) and (d) are blank because an explosive source was used to generate synthetic data.

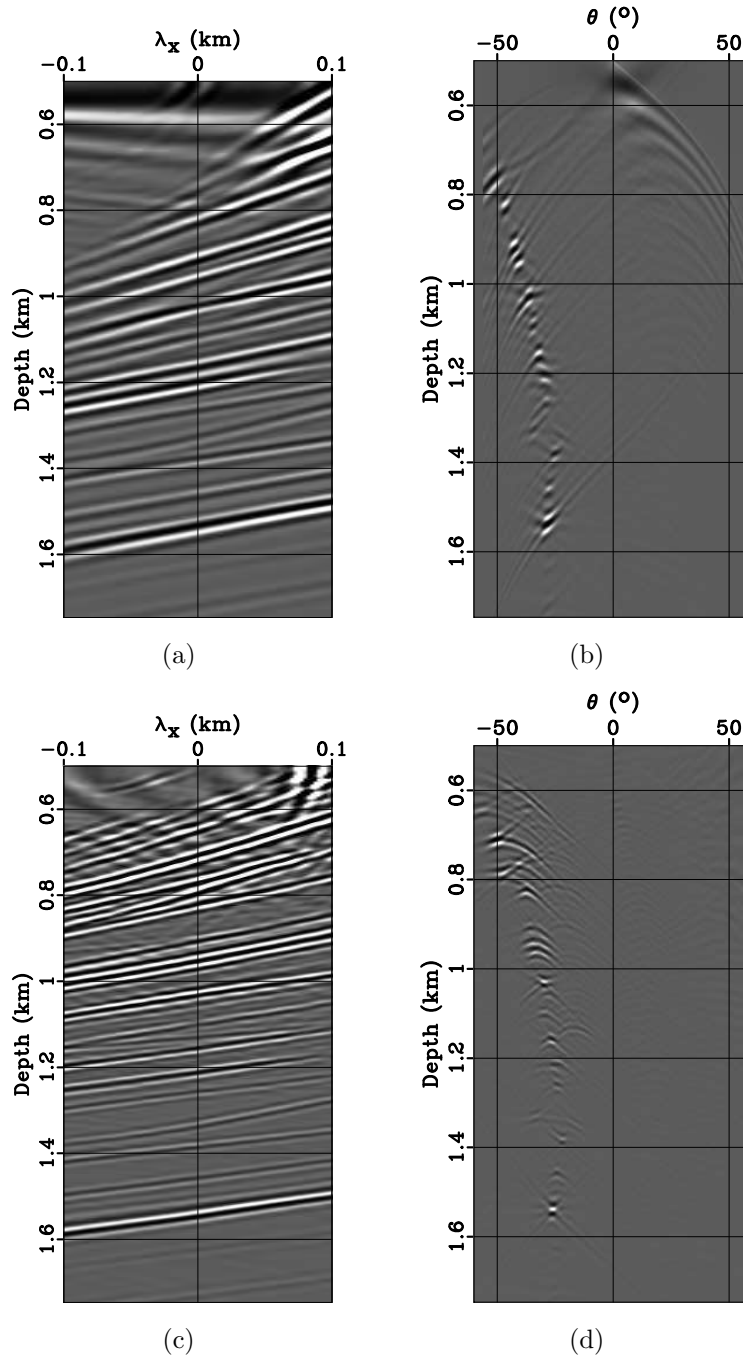


Figure 7: Horizontal cross-correlation lags for (a) PP and (c) PS reflections for the model in Figures 3(a) and 3(b). The source is at  $x = 6.75$  km, and the CIG is located at  $x = 6.5$  km. Panels (b) and (d) depict PP and PS angle gathers decomposed from the horizontal lag gathers in panels (a) and (c), respectively. As expected, PS angles are smaller than PP angles for a particular reflector due to smaller reflection angles.

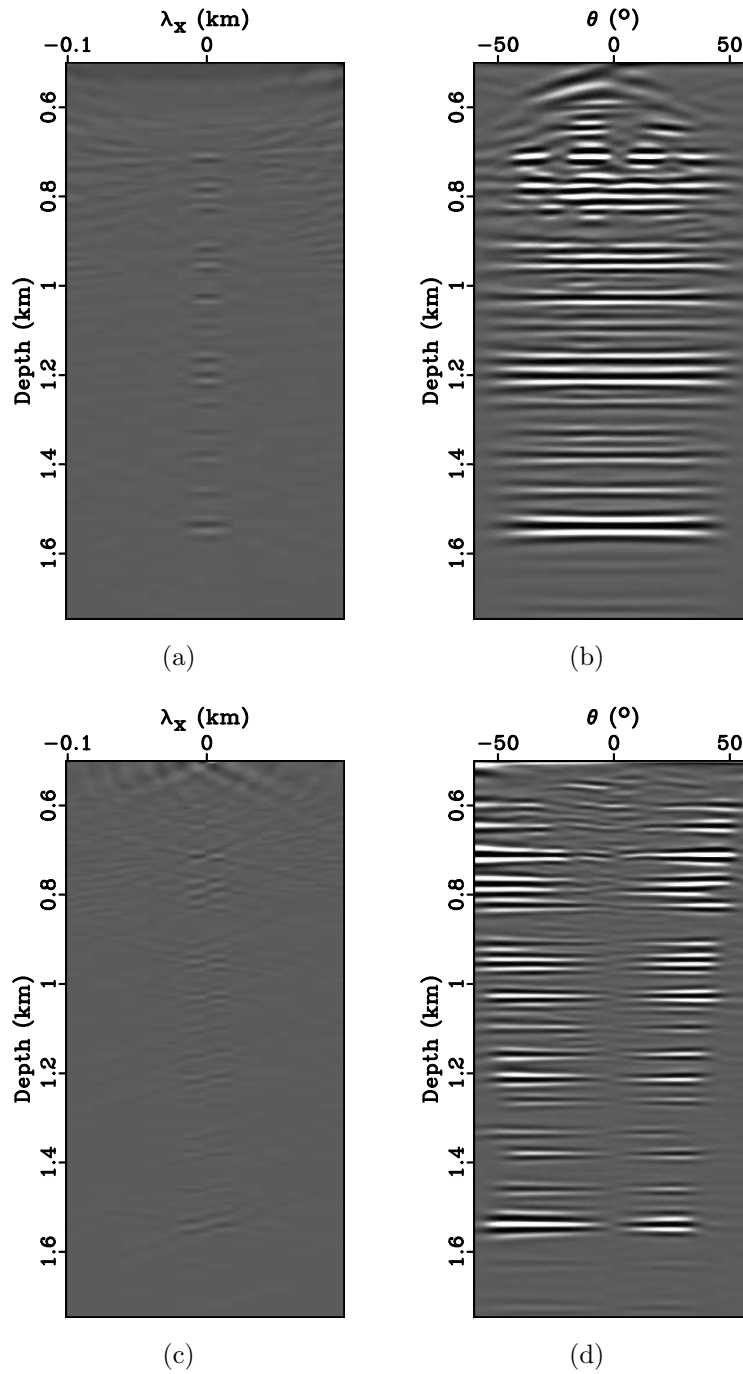


Figure 8: Horizontal cross-correlation lags for PP (a) and PS (c) reflections for the model in Figures 3(a) and 3(b). These CIGs correspond to 81 sources from  $x = 5.5$  to  $7.5$  km at  $z = 0.5$  km. The CIG is located at  $x = 6.5$  km. Panels (b) and (d) depict PP and PS angle gathers decomposed from the horizontal lag gathers in panels (a) and (c), respectively. Since the velocity used for imaging is correct, the PP and PS gathers are flat. The PP angle gathers do not change polarity at normal incidence, but the PS angle gathers change polarity at normal incidence.